High-Field Terahertz Bulk Photovoltaic Effect in Lithium Niobate

C. Somma,[1] K. Reimann,[1] C. Flytzanis,[2] T. Elsaesser,[1] and M. Woerner[1]
[1]*Max-Born-Institut für Nichtlineare Optik und Kurzzeitspektroskopie, 12489 Berlin, Germany*
[2]*Laboratoire Pierre Aigrain, École Normale Supérieure, F-75231 Paris, France*
(Received 12 November 2013; published 9 April 2014)

The terahertz (THz) response of the ferroelectric prototype material lithium niobate ($LiNbO_3$) is studied in the nonperturbative regime of light-matter interaction. Applying two-dimensional THz spectroscopy with few-cycle pulses of an amplitude $E \approx 100$ kV/cm and a center frequency of 2 THz, we dissect the overall nonlinear response into different orders in the electric field. The underlying nonlinear current is of interband character and consists of a strong low-frequency shift current (SC) and higher harmonics of the THz fundamental. The SC component originates from the lack of inversion symmetry and the strong interband decoherence for long electron trajectories in k space as shown by theoretical calculations.

DOI: 10.1103/PhysRevLett.112.146602 PACS numbers: 72.20.Ht, 77.80.-e, 77.84.Ek, 78.47.J-

The generation of charge and spin currents by irradiating solids with light represents an important type of light-matter interaction [1–8]. In semiconductors, electric currents have been induced by simultaneous nonlinear one- and two-photon excitation, generating an asymmetric carrier distribution in k space via the interference of quantum pathways and, thus, a unidirectional current [1–5]. A fundamentally different type of photoinduced electric current, the so-called bulk photovoltaic or photogalvanic effect, has been observed in bulk semiconductors and ionic ferroelectric crystals which lack inversion symmetry [9,10]. One-photon excitation of electrons in materials such as $LiNbO_3$, $BaTiO_3$ or $BiFeO_3$ gives rise to a short-circuit current through the uniformly illuminated solid [10–17].

The bulk photovoltaic effect has been described in the perturbative limit of light-matter interaction by a tensor relationship between the (real) short-circuit current density and the optical field in second order [18]. The absolute values of the tensor components have been determined for irradiation in the visible and photovoltages in the kilovolt range have been measured under open-circuit conditions [11,12,18]. In this limit, the bulk photovoltaic effect represents a second-order nonlinear optical response in the spectral range where the material absorbs light [17,19] . This effect must not be confused with the nonresonant second-order optical nonlinearity $\chi^{(2)}$ [20–23] which gives rise to a nonlinear optical polarization $P^{(2)}_{\mathrm{NL}}(t)$ and a rectification of the optical fields (OR), i.e., an $(\omega_i - \omega_j) \approx 0$ component. This low-frequency field is, however, not connected with a real electric current.

Different microscopic mechanisms have been proposed to explain the bulk photovoltaic effect. In a two-step model [10,13,15,24], absorption of a photon creates an electron-hole pair in the crystal with the electron populating a conduction band state. The subsequent intraband transport of electrons occurs in the locally asymmetric potential along the c axis of the crystal, resulting in a so-called shift current along this direction. The local asymmetry has been ascribed to different Nb-Fe^{2+} distances along the c direction [10]. Transport abruptly ends by electron trapping at an impurity ion. A different picture is based on a quantum mechanical description of the photocurrent in the basis of Bloch functions of different bands [25,26]. The calculations performed in the regime of perturbative light-matter interaction suggest a prominent role of off-diagonal interband matrix elements of the current operator, i.e., interband transitions (Eq. (37) of [26]), and of a damping of quantum interferences in generating the (real) photocurrent (Eq. (21) of [25]).

So far the bulk photovoltaic effect has been studied in the perturbative regime of light-matter interaction and on time scales much longer than the intrinsic microscopic carrier dynamics. In this Letter, we address this phenomenon in a totally different regime. First, we reduce the optical frequency to the THz range well below any electronic absorption in order to study field-induced rather than absorption-induced currents. Second, the light-matter interaction is driven into the nonperturbative regime where Zener tunneling [27] of electrons from the valence into the conduction band represents the major excitation mechanism instead. This regime is well beyond the perturbative interactions treated in [25,26].

Two-dimensional (2D) THz experiments on the time scale of the basic transport dynamics show that few-cycle transients polarized along the ferroelectric c axis with an amplitude $E \approx 100$ kV/cm generate highly nonlinear interband currents at various harmonics of the 2 THz fundamental and an optical shift current (SC) with the phase expected for a high field THz bulk photo-voltaic effect. The strong THz driving field allows valence electrons to explore a wide range of the Brillouin zone and generates large interband tunneling currents [28] with a net SC due to the lack of inversion symmetry. The irreversible character of

the driven interband transitions has its origin in the strong interband decoherence for long trajectories in k space as shown by theory.

In the experiments, we study an undoped single-domain $LiNbO_3$ crystal of a thickness of 50 μm. The ferroelectric c axis is perpendicular to its surface normal allowing for the electric field of the THz pulses to accelerate electrons along the c axis. The 2D THz experiments [29,30] are based on measuring the nonlinear response of the sample as a function of real time t and of the delay τ between the two phase-locked THz pulses interacting in a collinear geometry with the sample. A 2D Fourier transform provides the signal in frequency space as a function of the excitation frequency ν_τ and the detection frequency ν_t.

Details of the experiment have been presented in [31,32]. Two choppers synchronized to the pulse repetition rate allow for measuring the electric-field transients $E_{AB}(t,\tau)$ with both pulses A and B incident on the sample, as well as the pulses $E_A(t,\tau)$ [green curve in Fig. 1(a)] and $E_B(t)$ (blue curve) [33]. The nonlinear signal emitted from the sample [red curve in Fig. 1(a)] is the difference

$$E_{NL}(t,\tau) = E_{AB}(t,\tau) - E_A(t,\tau) - E_B(t). \quad (1)$$

In Figs. 1(b,c) we show experimental results for a full 2D-scan on $LiNbO_3$ driven by two THz pulses A and B polarized along the ferroelectric c axis. Panel (b) shows a contour plot of the electric field $E_{AB}(t,\tau)$ transmitted through the sample while panel (c) displays the nonlinear THz signal $E_{NL}(t,\tau)$. We observe a strong nonlinearly emitted electric field $E_{NL}(t=0,\tau=0) \approx 20$ kV/cm from the $LiNbO_3$ crystal. During the pulse overlap it reaches its maximum and points into the opposite direction of the driving field $E_{AB}(t=0,\tau=0)$.

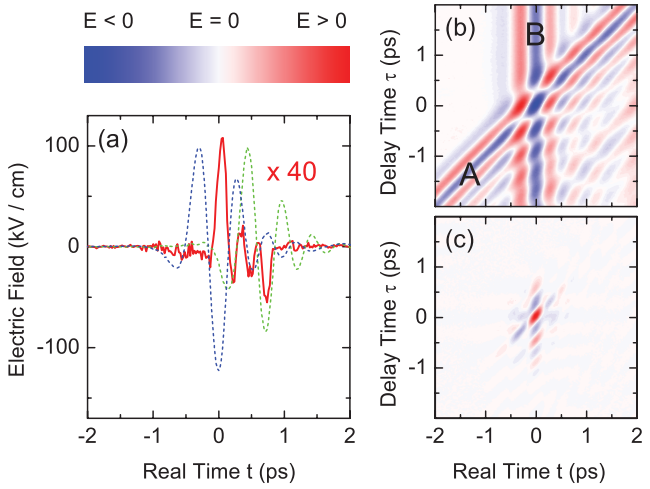

FIG. 1 (color). Experimental results for $LiNbO_3$ driven by two THz pulses A and B polarized along the ferroelectric c axis. (a) Electric fields E_A and E_B (dashed lines) of the THz pulses A and B separated by the time delay $\tau = 700$ fs and nonlinear signal field E_{NL} (solid line, cf. Eq. (1)) as a function of real time t. (b) Electric field $E_{AB}(t,\tau)$ transmitted through the sample as a function of t and τ. (c) Nonlinear THz signal $E_{NL}(t,\tau)$, reaching its maximum during the pulse overlap, i.e., $E_{NL}(t=0,\tau=0) = 20$kV/cm which is $\approx -0.1 E_{AB}(t=0,\tau=0)$.

The different contributions to the nonlinear signal can be separated in two-dimensional frequency space [29]. To this end, we calculated the 2D Fourier transform $E_{NL}(\nu_t,\nu_\tau)$ of the time-dependent nonlinear signal $E_{NL}(t,\tau)$ [Fig. 1(c)] as a function of the excitation (ν_τ) and detection (ν_t) frequencies. In Fig. 2, we plotted the (a) real part and (b) imaginary part of $E_{NL}(\nu_t,\nu_\tau)$ as a function of ν_t (abscissa) and ν_τ (ordinate). The amplitude of the real part is much larger than that of the imaginary part and displays distinct peaks at different frequency positions (ν_t,ν_τ). There are components at the fundamental THz frequency $\nu_t = \pm\nu_0 = \pm 2$ THz, at the second harmonic $\pm 2\nu_0$ (2nd in Fig. 2), at the third harmonic $\pm 3\nu_0$ (3rd), and at frequencies close to $\nu_t \approx 0$ (SC and OR) [33]. The OR peak originates from difference frequency mixing of the THz pulses $\nu_A - \nu_B \approx 0$ and vanishes at $\nu_t = 0$ as the dc component of the signal is not radiated and, thus, not detectable by free-space electrooptic sampling.

We first address the origins of the different nonlinear signals. The pump depletion signal [DP, Fig. 2(a)] stems from the fact that energy at the fundamental frequency is lost by transforming it into the nonlinearly generated light. For such new components, there are two types of potential source terms: (i) nonresonantly generated nonlinear polarizations $P^{(2)}(t)$ and $P^{(3)}(t)$ of second and third order in the THz driving fields and (ii) real currents of electrons generated and driven by the external THz field. A nonlinear

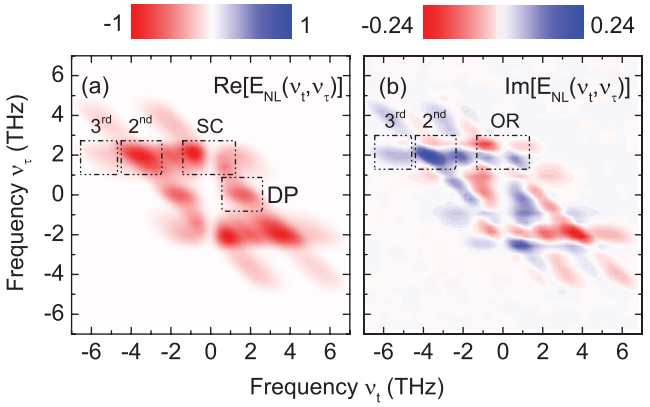

FIG. 2 (color). Two-dimensional Fourier transform of the time-dependent nonlinear signal shown in Fig. 1(c). The (a) real and (b) imaginary part of the electric field $E_{NL}(\nu_t,\nu_\tau)$ is shown as a function of the detection frequency ν_t and the excitation frequency ν_τ. The maximum amplitude of the real part is approximately 4 times larger than of the imaginary part. The rectangles indicate the shift current (SC), optical rectification (OR), the second harmonic (2nd), the third harmonic (3rd), and the depletion (DP) nonlinear signal components.

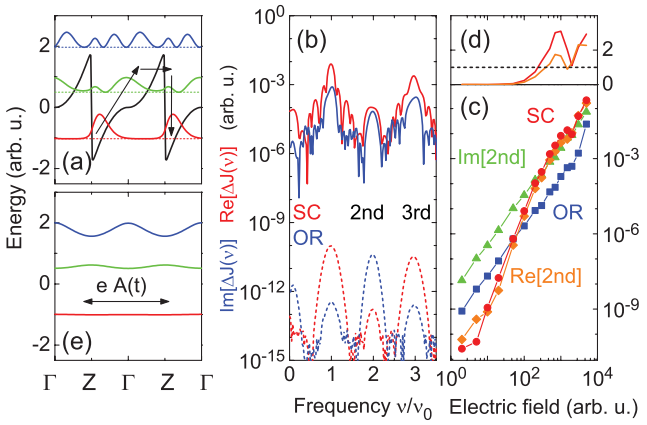

FIG. 3 (color). (a) Periodic potential (black line) of a one-dimensional model-crystal without inversion symmetry. The red, green and blue curves show the probability density $|\Psi_n(z)|^2$ of one valence and two conduction bands, respectively. The arrows sketch the directed electron transport by field-driven interband tunneling under the influence of decoherence making thereby real electron-hole pairs. (b) Calculated spectra of the real $\mathrm{Re}[\Delta J(\nu)]$ (red curves) and imaginary interband current $\mathrm{Im}[\Delta J(\nu)]$ (blue curves) in the model-crystal driven by a THz pulse (center frequency ν_0) with two amplitudes of $E = 1$ (dashed lines) and $E = 3000$ (solid lines). (c) Amplitudes of the second harmonic [$\mathrm{Re}[\Delta J_{2nd}]$ (diamonds), $\mathrm{Im}[\Delta J_{2nd}]$ (triangles)], shift current ΔJ_{SC} (circles) and optical rectification contribution ΔJ_{OR} (squares) of the calculated current $\Delta J(\nu)$ as a function of the field amplitude E. (d) Ratios $\mathrm{Re}[\Delta J_{2nd}]/\mathrm{Im}[\Delta J_{2nd}]$ (orange) and $\Delta J_{SC}/\mathrm{Im}[\Delta J_{2nd}]$ (red). (e) Band structure of the one-dimensional model crystal.

polarization source term [mechanism (i)] corresponds to an imaginary current $j_P(t) = dP^{(2,3)}(t)/dt$ and, thus, results in an imaginary field $E_{NL}(\nu_t, \nu_\tau)$. While Fig. 2(b) gives evidence of such contributions to the overall nonlinear response, in particular an OR contribution around $\nu_t = 0$, their amplitude is much smaller than the real part of $E_{NL}(\nu_t, \nu_\tau)$ not accounted for by nonlinear polarizations. The large real part of $E_{NL}(\nu_t, \nu_\tau)$ is a hallmark of a real nonlinear electron current density $j_{NL}(\nu_t, \nu_\tau)$; i.e., mechanism (ii) strongly dominates the nonlinear behavior. For a sample of a thickness d which is small compared to the THz wavelength λ, the time-dependent $E_{NL}(t, \tau)$ is given by $E_{NL}(t, \tau) = -(1/2)(Z_0 d) j_{NL}(t, \tau)$ with the vacuum impedance $Z_0 = 377\ \Omega$. A real SC requires the generation of free carriers in the material and, thus, this current is proportional to the intensity of $I_{THz} \propto |E_{THz}|^2$ of the THz pulses. The frequency spectrum $j_{NL}(\nu_t, \nu_\tau)$ reflects the dynamics of electron motion along the c axis of $LiNbO_3$ and contains SC components around zero frequency as well as harmonics up to–in principle–arbitrary order.

We now discuss the physical mechanisms underlying the high-field THz bulk photovoltaic effect in $LiNbO_3$. Key issues are the generation and the character of the current which underlies the SC and higher harmonics signals observed in the 2D spectrum. The electronic bandgap of our undoped $LiNbO_3$ crystal is much larger than $k_B T$ (k_B: Boltzmann's constant, T: sample temperature) and both the thermally excited and a potential residual density of free electrons are orders of magnitude too small to drive a THz intraband current which emits the measured strong THz fields. Instead, the nonlinear current is generated by field-induced interband tunneling of electrons from the valence into the conduction band, a mechanism introduced by Zener [27].

The basic mechanism of the THz-induced SC is as follows. The electric field of the THz pulse $E(t)$ has two effects on the wave function at wave vector k of a valence electron (cf. Eq. (8) and Fig. 7 of [28]). First, it creates a coherent superposition of the valence band state with various conduction band states. Since the cell periodic part of the Bloch functions is different for different bands such a coherent superposition is typically connected to a charge transfer between neighboring atoms (ions) as shown recently in femtosecond x-ray diffraction experiments [34,35]. Second, $E(t)$ drives the wave vector k of the coherent interband polarization wave packet back and forth within the Brillouin zone, thereby creating a large spatial separation Δx between the electron and the hole part within the "nonclassical" wave packet of several 100 nanometers. At finite temperatures (Eq. (8) of [28]) such a "nonclassical" wave packet experiences a huge decoherence rate even for weak intraband damping rates (Fig. 8(b) of [28]) thereby creating incoherent electron-hole pairs from those being "virtually" present by the induced coherent polarization. In crystals with inversion symmetry this mechanism leads just to a field-induced generation of carriers in various conduction bands. In $LiNbO_3$ which lacks inversion symmetry, however, the charge displacement of coherent superpositions [34,35] has a preferred direction, connecting the electron-hole generation rate (Fig. 8(a) of [28]) to a directed SC $j_{SC}(t)$.

To analyze the basic physics in more detail, we extended the theory of Refs. [25,26] into the nonperturbative regime and introduced a more sophisticated description of interband decoherence by using our model developed for THz-induced interband tunneling in GaAs [28]. The model is based on a plane wave approach using a finite set of reciprocal lattice vectors (see Eqs. (9) to (11) of [28]). The time evolution of the density matrix is obtained from the Liouville equation,

$$\frac{d\rho}{dt} = \frac{1}{i\hbar}[H(t), \rho] - \Gamma(t, \rho). \tag{2}$$

The term $\Gamma(t, \rho)$ represents a relaxation operator, accounting for decoherence (off-diagonal terms) and population relaxation (diagonal terms) [36]. In contrast to simplified concepts, the decoherence rate in Eq. (2) is not constant in time, since it depends on the time-dependent electron-hole separation $\Delta x_{i,j}(t) = x_i(t) - x_j(t)$ within a "nonclassical" interband polarization wave packet $\rho_{i,j}$ between bands i

and j. Such nonclassical wave packets experience extremely high decoherence rates at finite temperatures T [37,38],

$$\Gamma_{i,j}(t) = \tau_{\mathrm{m}}^{-1} \frac{m k_{\mathrm{B}} T [\Delta x_{i,j}(t)]^2}{\hbar^2}. \quad (3)$$

Here, τ_{m} is the momentum relaxation time, responsible, e.g., for low-field transport. The decoherence term and the nonperturbative light-matter interaction require a numerical evaluation of Eq. (3) for each interband polarization $\rho_{i,j}$ individually according to the trajectories within bands i and j.

To illustrate the SC physics in $LiNbO_3$ we applied the interband tunneling picture [28] to a one-dimensional model crystal lacking inversion symmetry. In Fig. 3(a) we show the periodic potential (black line) together with the probability density $|\Psi_n(z)|^2$ of one valence and two conduction bands at $k = 0$ (red, green and blue curves with separate dashed base lines). We calculate THz-induced nonlinear interband currents in this system and the properties of THz radiation emitted by them [39]. For an adequate comparison with the nonlinear current generating the measured electric fields (1), we determine the difference current $\Delta J_E(\nu) = J_E(\nu) - 2J_{E/2}(\nu)$ created by two THz-fields (center frequency ν_0) where $J_E(\nu)$ and $J_{E/2}(\nu)$ corresponds to the current with both and with individual THz pulses present. Fig. 3(b) shows the calculated spectra of the real part $\mathrm{Re}[\Delta J(\nu)]$ (red curves) and the imaginary part $\mathrm{Im}[\Delta J(\nu)]$ (blue curves) of the difference current for two amplitudes of $E = 1$ (dashed lines) and $E = 3000$ (solid lines), the latter corresponding approximately to our experimental situation. In Fig. 3(c) we show the amplitudes of the $\nu \approx 0$ real ΔJ_{SC} (circles) and imaginary ΔJ_{OR} (squares) as well as the second harmonic $\mathrm{Re}[\Delta J_{2\mathrm{nd}}]$ (diamonds) and $\mathrm{Im}[\Delta J_{2\mathrm{nd}}]$ (triangles) as a function of the field amplitude E.

For low field strengths [$E = 1$, dashed lines in Fig. 3(b)] we observe a nonlinear response according to the standard picture of nonlinear optics in the $\chi^{(2)}$ limit; i.e., the imaginary current (blue curves) dominates and we observe the expected field strength dependence. In particular, the $\nu \approx 0$ contribution of the calculated current is dominated by its imaginary part $\mathrm{Im}[\Delta J(\nu \approx 0)]$ [OR: squares in Fig. 3(c)] as expected for an induced nonlinear polarization following the intensity profile of the driving THz pulse, i.e., a quadratic dependence on E similar to the second harmonic $\mathrm{Im}[J_{2\mathrm{nd}}]$ contribution [triangles in Fig. 3(c)].

When increasing the field strength [$E = 3000$ (solid lines) in Fig. 3(b)] we find a drastic qualitative change of the nonlinear response. In this new regime, the transient vector potential $A(t) = \int_{-\infty}^{t} dt' E(t')$ of the driving THz field allows the valence electrons to explore a significant part of the Brillouin zone up to its boundary (Z point) [Fig. 3(e)]. As a consequence one drives the system into the nonperturbative regime of light-matter interaction. It is now dominated by real interband currents $\mathrm{Re}[\Delta J(\nu)]$ [red curves in Fig. 3(b)] with a frequency spectrum displaying many harmonics of the basic THz driving frequency. While systems with inversion symmetry can exclusively emit the odd harmonics, the lack of an inversion center in $LiNbO_3$ [or in our model potential shown in Fig. 3(a)]) allows for a second (somewhat weaker) series of even harmonics both decaying almost exponentially as a function of the harmonic order (not shown).

For the strength of the SC, interband decoherence according to Eqs. (2) and (3) plays a crucial role. While for short trajectories in k space [$E = 1$ (dashed lines) in Fig. 3(b)] interband decoherence has an almost negligible influence on the generation of various harmonics, it makes a drastic change of amplitude of the real SC component J_{SC} for long trajectories in k space [red circles in Fig. 3(c)]. It starts with an amplitude which is smaller than that of J_{OR} (squares). However, it rises steeply once entering the nonperturbative regime of light-matter interaction, getting an even higher amplitude than $\mathrm{Im}[J_{2\mathrm{nd}}]$ for $E > 500$ as shown in Fig. 3(d) in agreement with the experimental 2D spectrum in Fig. 2. In this regime the shift current has exactly the phase expected for a high field THz bulk photovoltaic effect as observed in our experiments [Fig. 2(a)]. Switching off the interband decoherence in our calculations suppresses the shift current J_{SC} completely (not shown), since the absence of decoherence does not allow for irreversible generation of free carriers by interband tunneling.

In conclusion, we have reported the first observation of a high field bulk photovoltaic effect in $LiNbO_3$ under conditions of a nonperturbative interaction with strong terahertz fields polarized along the crystal's c axis. Two-dimensional THz spectra measured with phase-locked pulses of an amplitude of 100 kV/cm reveal the simultaneous occurrence of a rectification signal close to zero frequency and of second- and third-harmonic signals. A nonlinear interband current which is generated by interband tunneling and driven along the c axis in the strong THz field represents the source of the nonlinear signals. The new basic generation mechanism introduced here allows for coherently controlling the shift current by a tailored ultrafast THz driving field, allowing for new functional processes in high speed ferroelectric devices.

We acknowledge financial support by the Deutsche Forschungsgemeinschaft: WO 558/13-1 and RE 806/9-1.

[1] E. Dupont, P. B. Corkum, H. C. Liu, M. Buchanan, and Z. R. Wasilewski, Phys. Rev. Lett. **74**, 3596 (1995).
[2] R. Atanasov, A. Haché, J. L. P. Hughes, H. M. van Driel, and J. E. Sipe, Phys. Rev. Lett. **76**, 1703 (1996).
[3] A. Haché, Y. Kostoulas, R. Atanasov, J. L. P. Hughes, J. E. Sipe, and H. M. van Driel, Phys. Rev. Lett. **78**, 306 (1997).

[4] D. Cŏte, J. M. Fraser, M. DeCamp, P. H. Bucksbaum, and H. M. van Driel, Appl. Phys. Lett. **75**, 3959 (1999).
[5] L. Costa, M. Betz, M. Spasenović, A. D. Bristow, and H. M. van Driel, Nat. Phys. **3**, 632 (2007).
[6] M. Bieler, K. Pierz, U. Siegner, and P. Dawson, Phys. Rev. B **73**, 241312(R) (2006).
[7] S. D. Ganichev, E. L. Ivchenko, V. V. Bel'kov, S. A. Tarasenko, M. Sollinger, D. Weiss, W. Wegscheider, and W. Prettl, Nature (London) **417**, 153 (2002).
[8] M. J. Stevens, A. L. Smirl, R. D. R. Bhat, A. Najmaie, J. E. Sipe, and H. M. van Driel, Phys. Rev. Lett. **90**, 136603 (2003).
[9] V. I. Belinicher and B. I. Sturman, Sov. Phys. Usp. **23**, 199 (1980).
[10] A. M. Glass, D. von der Linde, and T. J. Negran, Appl. Phys. Lett. **25**, 233 (1974).
[11] V. M. Fradkin and R. M. Magomadov, Pis'ma Zh. Eksp. Teor. Fiz. **30**, 723 (1979) [JETP Lett. **30**, 686 (1979)].
[12] H. G. Festl, P. Hertel, E. Krätzig, and R. von Baltz, Phys. Status Solidi B **113**, 157 (1982).
[13] R. Grousson, M. Henry, S. Mallick, and S. L. Xu, J. Appl. Phys. **54**, 3012 (1983).
[14] G. Dalba, Y. Soldo, F. Rocca, V. M. Fridkin, and P. Sainctavit, Phys. Rev. Lett. **74**, 988 (1995).
[15] V. M. Fridkin, Kristallografiya **46**, 722 (2001) Crystallogr. Rep. (Transl. Kristallografiya) **46**, 654 (2001)].
[16] F. Luedtke, K. Buse, and B. Sturman, Phys. Rev. Lett. **109**, 026603 (2012).
[17] S. M. Young and A. M. Rappe, Phys. Rev. Lett. **109**, 116601 (2012).
[18] R. S. Weis and T. K. Gaylord, Appl. Phys. A **37**, 191 (1985).
[19] J. E. Sipe and A. I. Shkrebtii, Phys. Rev. B **61**, 5337 (2000)
[20] J. A. Giordmaine and R. C. Miller, Phys. Rev. Lett. **14**, 973 (1965).
[21] I. Breunig, M. Falk, B. Knabe, R. Sowade, K. Buse, P. Rabiei, and D. H. Jundt, Appl. Phys. Lett. **91**, 221110 (2007).
[22] I. Shoji, T. Kondo, A. Kitamoto, M. Shirane, and R. Ito, J. Opt. Soc. Am. B **14**, 2268 (1997).
[23] A. Riefer, S. Sanna, A. Schindlmayr, and W. G. Schmidt, Phys. Rev. B **87**, 195208 (2013).
[24] A. M. Glass, D. von der Linde, D. H. Auston, and T. J. Negran, J. Electron. Mater. **4**, 915 (1975).
[25] W. Kraut and R. von Baltz, Phys. Rev. B **19**, 1548 (1979).
[26] R. von Baltz and W. Kraut, Phys. Rev. B **23**, 5590 (1981).
[27] C. Zener, Proc. R. Soc. A **145**, 523 (1934).
[28] W. Kuehn, P. Gaal, K. Reimann, M. Woerner, T. Elsaesser, and R. Hey, Phys. Rev. B **82**, 075204 (2010).
[29] W. Kuehn, K. Reimann, M. Woerner, and T. Elsaesser, J. Chem. Phys. **130**, 164503 (2009).
[30] W. Kuehn, K. Reimann, M. Woerner, T. Elsaesser, and R. Hey, J. Phys. Chem. B **115**, 5448 (2011).
[31] M. Woerner, W. Kuehn, P. Bowlan, K. Reimann, and T. Elsaesser, New J. Phys. **15**, 025039 (2013).
[32] K. Reimann, Rep. Prog. Phys. **70**, 1597 (2007).
[33] The pulses *A* and *B* have a slightly different center frequency, and frequencies higher than the third harmonic cannot be detected because of the limited transparency of the ZnTe crystal used for electrooptic sampling.
[34] J. Stingl, F. Zamponi, B. Freyer, M. Woerner, T. Elsaesser, and A. Borgschulte, Phys. Rev. Lett. **109**, 147402 (2012).
[35] V. Juve, M. Holtz, F. Zamponi, M. Woerner, T. Elsaesser, and A. Borgschulte, Phys. Rev. Lett. **111**, 217401 (2013).
[36] C. Flytzanis, Proc. SPIE Int. Soc. Opt. Eng. **7747**, 774713 (2011).
[37] W. H. Zurek, Phys. Today **44**, 36 (1991).
[38] A. O. Caldeira and A. J. Leggett, Physica (Amsterdam) **121A**,587 (1983).
[39] Our calculations show that the interband current dominates by two orders of magnitude the intraband current originating from the intraband motion of THz-generated electron-hole pairs.